

On the accretion-induced QNM excitation of a Schwarzschild black hole

Alessandro Nagar^{1,3}, Olindo Zanotti^{2,3}, José A. Font³ and Luciano Rezzolla^{4,5,6}

¹*Dipartimento di Fisica and INFN, Politecnico di Torino, Torino, Italy*

²*Dipartimento di Astronomia e Scienza dello Spazio Università di Firenze, Firenze, Italy*

³*Departamento de Astronomía y Astrofísica, Universidad de Valencia, Valencia, Spain*

⁴*Max-Planck-Institut für Gravitationsphysik, Albert-Einstein-Institut, Potsdam-Golm, Germany*

⁵*SISSA, International School for Advanced Studies and INFN, Trieste, Italy and*

⁶*Department of Physics, Louisiana State University, Baton Rouge, USA*

(Dated: November 20, 2021)

By combining the numerical solution of the nonlinear hydrodynamics equations with the solution of the linear inhomogeneous Zerilli-Moncrief and Regge-Wheeler equations we investigate the properties of the gravitational radiation emitted during the axisymmetric accretion of matter onto a Schwarzschild black hole. The matter models considered include quadrupolar dust shells and thick accretion disks, permitting us to simulate situations which may be encountered at the end stages of stellar gravitational collapse or binary neutron star merger. We focus on the interference pattern appearing in the energy spectra of the emitted gravitational waves and on the amount of excitation of the quasi-normal modes of the accreting black hole. We show that, quite generically in the presence of accretion, the black hole ringdown is not a simple superposition of quasi-normal modes, although the fundamental mode is usually present and often dominates the gravitational-wave signal. We interpret this as due to backscattering of waves off the non-exponentially decaying part of the black hole potential and to the finite spatial extension of the accreting matter. Our results suggest that the black hole QNM contributions to the full gravitational wave signal should be extremely small and possibly not detectable in generic astrophysical scenarios involving the accretion of extended distributions of matter.

PACS numbers: 04.30.Db, 04.40.Dg, 95.30.Lz, 98.62.Mw

I. INTRODUCTION

It is well known within the framework of black-hole perturbation theory [1, 2, 3] that quasi-normal modes (QNMs) (i.e., exponentially damped harmonic oscillations) dominate the gravitational-wave response of a non-spherically distorted black hole if the corresponding frequencies are part of the Fourier spectrum of the external source that moved the hole away from its equilibrium state. This perturbation is then radiated away in form of gravitational radiation until the black hole returns to its unperturbed, quiescent state. In practice, the QNMs excitation is triggered if the frequency of the perturbing agent (e.g. an external matter source moving close to the black hole) is sufficiently close to the fundamental frequencies of the black hole, which then acts as an excited oscillator. As a result, the QNMs and in particular the fundamental mode (which is the one at the highest frequency and with the smallest damping time) represent the main feature of the gravitational waves emission only for a sufficiently compact perturbation; i.e., for sources whose characteristic scale is comparable with the width of the peak of the potential.

These results are well-known since the early studies of Press [4] (see also Vishveshwara [5]), who considered the scattering of Gaussian gravitational-wave packets off a Schwarzschild black hole and noticed that the excitation of the QNMs of the black hole is more efficient for very narrow packets. Approximate relations to compute the efficiency of excitation of the various QNMs were introduced by Leaver [6] and by Andersson [7] for Gaussian pulses initial data with variable width. Since the QNMs spectrum is entirely determined by the black hole properties (i.e., mass, spin and charge), it is expected that the detection of the QNMs ringdown would provide a unique opportunity to unveil the phys-

ical properties of a black hole. For this reason, the excitation of black hole QNMs have been studied in various astrophysical scenarios, such as the gravitational collapse of a (rotating) neutron star to a black hole or the collision of two black holes. The presence of the QNMs in these situations has been confirmed either through the use of perturbation theory with various degrees of sophistication [8, 9, 10], or through fully relativistic numerical simulations [11, 12, 13, 14, 15].

However, under more general and realistic conditions, such as the excitation of the QNMs by accretion of matter, and that may be encountered in gravitational stellar collapse or binary neutron star mergers, the gravitational-wave response of a black hole can be more complex. For instance, the simulations performed by [16, 17, 18] showed that the gravitational-wave signal is not simply given by the superposition of exponentially-damped sinusoids at the QNMs frequencies and that, in some cases, the QNM ringing is only weakly excited and analysis in the frequency domain are needed [19]. On the other hand, “backscattering” effects related to the slowly-decaying features of the scattering potential and interference effects turn out to play a crucial role for the correct interpretation of the results; a detailed discussion of these effects can be found in Ref. [18].

In the case of a Schwarzschild black hole of mass M , we recall that the appearance of QNMs ringing is related to the peak of the curvature potential (also referred to as the Zerilli or Regge-Wheeler potential), that is located at $r \simeq 3M$; the backscattering, on the other hand, is related to the fact that the curvature potential decays as r^{-2} for $r \rightarrow \infty$. This behavior is responsible for the late time power-law tail $t^{-(2\ell+3)}$ of the gravitational-wave signal, where ℓ refers to the radiation multipole.

Therefore, while early-time ringing is the result of a su-

perposition of exponentially damped sinusoids, and is dominated by the fundamental quasi-normal mode, at later times the ringing dies out and the signal is dominated by tail effects. However, in the transition from the “ringdown” to the “tail” phase, additional oscillations appear that cannot be attributed to any of the two regimes and that also seem to depend on the choice of the initial data (see [2, 3]). As we shall show in this paper for a broad sample of initial data, there could be intermediate regimes where the “ringdown” and the “tail” terms of the potential produce competing effects, so that the QNMs ringing and the backscattering effects can overlap, generating complex waveforms. These effects were first noticed in Refs. [16, 17], although not discussed in detail there.

In a recent paper [17], hereafter Paper I, a general analysis of the gravitational radiation emitted as a result of anisotropic accretion of matter shells onto nonrotating black holes and neutron stars was presented. That investigation made use of a procedure that combines the solution of the linearized Einstein equations for the metric perturbations with fully nonlinear hydrodynamics simulations. Although the study of black hole perturbations produced by infalling matter has a long history and rich literature [20, 21, 22], the approach outlined in Paper I proved to be useful for a number of reasons: *i*) it provided additional information on the black-hole’s response to the dynamics of point-like particles in the vicinity of black holes; *ii*) it helped understanding the basic black-hole’s response to extended matter perturbations; *iii*) it represented an effective way of studying black-hole physics in a linear regime without having to resort to full-scale numerical relativity simulations.

One of the main results of Paper I was that, in the idealized accretion processes considered, most of the energy is released at frequencies lower than that of the fundamental quasi-normal mode (QNM) of the black hole, the spectrum consisting of a complex pattern, mostly produced during the accretion process rather than in the ringdown phase. More precisely, the gravitational-wave emission was found to be dominated by a collection of interference “fringes” at frequencies of about a few hundred Hz, rather than by a single monochromatic peak at the (higher) frequency of the fundamental mode of the black hole. Moreover, the width of these fringes was found to decrease rapidly with the initial position of the matter source. These results, which were already observed in other works [8, 23] in the case of a point-like particle falling onto a Schwarzschild black hole, also showed that the appearance of interference fringes in the energy spectra is much larger when the accreting matter is a shell of finite size and that the efficiency in gravitational-wave emission is much reduced, becoming almost two orders of magnitude smaller than in the case of point-like particles. An important feature of the calculations carried out in Paper I was the minimization of the initial gravitational-wave content; this turned out to be crucial to illustrate that the interference pattern was mainly due to the finite radial extension of the accreting source.

The aim of the present paper is twofold. Firstly, we intend to complete the discussion started in Paper I on accreting quadrupolar shells onto a Schwarzschild black hole by extending the parameter space of the initial models and by analyzing their impact on the gravitational-wave emission. In particu-

lar we study how the energy emitted in gravitational waves, and the corresponding spectra, depend on the compactness of the shells as well as on their initial locations. In doing so we show that, for a finite-size source, the ringing of the black hole is much more complex than a simple superposition of QNMs and that the energy spectra (and in particular the interference fringes) are dependent on the choice of the initial data.

Secondly, we improve the astrophysical relevance of our study by analyzing the gravitational radiation produced by thick accretion disks [24, 25] which accrete onto the black hole on dynamical timescales. We recall, in fact, that quasi-periodic oscillations of thick accretion disks (or tori) orbiting around Schwarzschild or Kerr black holes have been recently addressed as promising sources of gravitational waves [18, 26, 27, 28, 29] in the kHz range.

The paper is organized as follows: in Sec. II we review the theory of odd- and even-parity nonspherical perturbations of Schwarzschild spacetime, writing the inhomogeneous Zerilli-Moncrief and Regge-Wheeler equations in a form suitable for time-domain calculations. Sec. III briefly describes the numerical approach adopted for the simulations, while Sec. IV is devoted to the discussion of the results. Finally, Sec. V provides a summary of the most important results and presents our conclusions. Unless otherwise specified, we choose geometrized units ($c = G = 1$), and the black hole mass M is the unit of length.

II. GAUGE-INVARIANT PERTURBATIONS OF THE SCHWARZSCHILD METRIC

A. Odd and even-parity master equations

The theory of gauge-invariant nonspherical metric perturbations of a Schwarzschild spacetime has a long history which has been recently reviewed in Refs. [30, 31]. We here simply recall that in this approach the spacetime metric $g_{\mu\nu}$ is described by the background Schwarzschild metric $g_{\mu\nu}^{(0)}$ plus a nonspherical perturbation $h_{\mu\nu}$. As a result of the spherical symmetry, $h_{\mu\nu}$ can be expanded in three odd-parity and seven even-parity multipoles

$$g_{\mu\nu} = g_{\mu\nu}^{(0)} + \sum_{l=0}^{\infty} \sum_{m=-l}^l (h_{\mu\nu}^{\ell m})^{(o)} + (h_{\mu\nu}^{\ell m})^{(e)}, \quad (1)$$

with the odd multipoles transforming as $(-1)^{l+1}$ and the even ones as $(-1)^l$ under a parity transformation $(\theta, \varphi) \rightarrow (\pi - \theta, \pi + \varphi)$. The presence of matter around the black hole is accounted through a “source” term in the linearized Einstein’s equations, represented by a stress energy tensor $t_{\mu\nu}$ which can also be expanded in multipoles. From the multipoles of the perturbed metric, it is possible to build odd, $\Psi_{\ell m}^{(o)}$, and even-parity, $\Psi_{\ell m}^{(e)}$, gauge invariant quantities which are solution of two equations, the Regge-Wheeler [32] and Zerilli-Moncrief [33, 34] equations, respectively and whose expression in Schwarzschild coordinates is given by

$$\partial_t^2 \Psi_{\ell m}^{(o/e)} - \partial_{r_*}^2 \Psi_{\ell m}^{(o/e)} + V_l^{(o/e)} \Psi_{\ell m}^{(o/e)} = S_{\ell m}^{(o/e)}. \quad (2)$$

Here the upper indices refer to the odd and even case respectively and $r_* = r + 2M \log[r/(2M) - 1]$ is the “tor-toise” coordinate (see Refs. [31, 35] for the most general covariant form of these equations). Explicit expressions for the scattering potentials $V_l^{(o)}$ and $V_l^{(e)}$ are well known and can be found, for example, in Ref. [30]. The source terms in Schwarzschild coordinates can also be found in [17, 30], while the corresponding expressions valid for any coordinate slicing of Schwarzschild spacetime are reported in detail in Ref. [31]. Once $\Psi_{\ell m}^{(e)}$ and $\Psi_{\ell m}^{(o)}$ are known, the gravitational-wave amplitude can be computed as

$$h_+ - ih_\times = \frac{1}{r} \sum_{l \geq 2, m} \sqrt{\frac{(l+2)!}{(l-2)!}} \left(\Psi_{\ell m}^{(e)} + i \Psi_{\ell m}^{(o)} \right) {}_{-2}Y^{\ell m}, \quad (3)$$

where ${}_{-2}Y^{\ell m} \equiv {}_{-2}Y^{\ell m}(\theta, \varphi)$ are the 2 spin-weighted spherical harmonics [36] and the emitted power in gravitational waves is simply given by

$$\frac{dE}{dt} = \frac{1}{16\pi} \sum_{l \geq 2, m} \frac{(l+2)!}{(l-2)!} \left(\left| \dot{\Psi}_{\ell m}^{(o)} \right|^2 + \left| \dot{\Psi}_{\ell m}^{(e)} \right|^2 \right), \quad (4)$$

where the overdot refers to a derivative with respect to the Schwarzschild coordinate time.

B. Initial data

Specifying suitable initial data for nonspherical metric perturbations taking place in astrophysical events is not trivial. The standard approach, in the case of even-parity perturbations, exploits the fact that $\Psi_{\ell m}^{(e)}$ can be written in terms of two gauge-invariant multipoles, namely the perturbed conformal factor $k_{\ell m}$ and the gravitational-wave degree of freedom $\chi_{\ell m}$ as introduced, for instance, in Eq. (8) of Paper I and whose relationship with the Zerilli-Moncrief equation is given by Eq. (18) of the same reference [30, 37]. As a result, the perturbed Hamiltonian equation and the equation for the momentum constraint, i.e., Eqs. (45) and (46) of [30], provide a system of coupled ordinary differential equations for the unknowns ($k_{\ell m}$, $\chi_{\ell m}$, $\partial_t k_{\ell m}$, and $\partial_t \chi_{\ell m}$). The indetermination inherent in the solution of this system can be overcome, for example, by assuming $\chi_{\ell m} = \beta k_{\ell m}$ [23], where $\beta \geq 0$, so that the Hamiltonian constraint simply reads

$$\partial_{r_*}^2 k_{\ell m} + \left[\frac{2}{r} - \frac{5M}{r^2} - \beta \left(\frac{1}{r} - \frac{2M}{r^2} \right) \right] \partial_{r_*} k_{\ell m} - \left(1 - \frac{2M}{r} \right) \left[\frac{\Lambda}{r^2} + \beta \frac{\Lambda + 2}{2r^2} \right] k_{\ell m} = -8\pi T_{00}^{\ell m}, \quad (5)$$

where $\Lambda = \ell(\ell + 1)$ and $T_{00}^{\ell m}$ are the multipoles of the energy density t_{00} of the matter source according to the multipolar decomposition given by Eq. (13) of Paper I (see also Ref. [37]). The case $\beta = 0$ corresponds to conformally flat initial data, since in this case the perturbed metric in isotropic coordinates is the Schwarzschild one modulo a conformal transformation.

Depending on the problem under investigation, we can either choose initial conditions that are time-symmetric (i.e., for which $\partial_t k_{\ell m} = \partial_t \chi_{\ell m} = 0$) or not. In the first case, if the Hamiltonian constraint is satisfied, the momentum constraint is automatically satisfied too. In the second case, on the other hand, the momentum constraint must also be solved for $\partial_t k_{\ell m}$ if we provide a suitable ansatz for $\partial_r \chi_{\ell m}$.

Whether it is possible to use time-symmetric initial data depends essentially on the astrophysical scenario under investigation and thus on the form of the stress-energy tensor of the matter, whose multipoles appear as sources in the Hamiltonian and momentum constraint equations. Clearly, time-symmetry is satisfied for matter configurations in equilibrium, or initially at rest and subsequently falling radially; in this case only the numerical solution of the Hamiltonian constraint is needed.

This is the case, for example, of dust shells initially at rest at a finite radius. Because this configuration is intrinsically non time symmetric, it will inevitably produce spurious radiation. A way to minimize the latter is to freeze the sources of the perturbation equations up until the radiation has left the grid. This is the approach we will follow in most of our simulations.

III. NUMERICAL FRAMEWORK

The numerical approach adopted in our simulations is the same as the one described in Paper I. We only recall here that our hybrid approach implies the solution of both the nonlinear, relativistic hydrodynamics equations on a fixed Schwarzschild background, in the two spatial dimensions r and θ (since we restrict ourselves to axisymmetric flows), and of the Regge-Wheeler and Zerilli-Moncrief, in the radial direction r_* . Such “test-fluid approximation” is valid as long as the mass of the accretion flow is much smaller than the mass of the black hole; in our simulations this mass ratio is $\lesssim 10\%$.

The hydrodynamics equations, once cast in conservation form, are solved using Godunov-type methods based on Riemann solvers (see e.g. [38] and references therein), while Eqs. (2) can be written as a first-order hyperbolic system over a one-dimensional (1D) grid expressed in terms of the radial coordinate r_* and solved with some standard finite-difference method such as Lax-Wendroff (see Paper I for details).

The computational domain used for the hydrodynamical evolution consists of $N_r \times N_\theta$ grid-points, geometrically distributed along r [that is, with grispacing $\Delta r_{j+1} = \alpha \Delta r_j$ with $\alpha \gtrsim 1$] and uniformly distributed along θ . When we evolve quadrupolar shells of dust plunging from large distances we set $N_r = 2000$ and $N_\theta = 20$, while for the evolution of fluid accretion disks we use $N_r = 300$ and $N_\theta = 150$ to reach the desired truncation error. The hydrodynamical grid extends from a point slightly outside the event horizon up to a finite radius, that depends on the initial data, much smaller than the extraction radius. At the inner boundary we impose inflowing boundary conditions, while at the outer one we fix the conditions of a tenuous stationary spherical atmosphere.

The radial grid used for the time evolution of the Regge-Wheeler and Zerilli-Moncrief equations, on the other hand, is much more extended in radius than the hydrodynamical one

and overlaps with the latter. To avoid spurious boundary effects, the 1D grid typically extends from $-2000 M$ to $5000 M$ and is covered by $\sim 10^5$ cells. At the inner and outer boundary of this grid we use standard Sommerfeld outgoing conditions. We stress that, due to the long-range action of the potential, these conditions are not completely non-reflecting, which is the reason why we still need large grids to properly capture the late time power-law decay of the waveforms (see below). We recall in passing that exactly non-reflecting boundary condition for the Zerilli-Moncrief and Regge-Wheeler equations have been recently proposed in [39].

While the gravitational waveforms are extracted using both the Regge-Wheeler and Zerilli-Moncrief equations, we also use as a comparison the Newtonian quadrupole formula to compute the amount of gravitational waves emitted. We use the modified definition of the quadrupole moment proposed in Ref. [18] and which reads

$$I = 2\pi \int_{-1}^1 dz \int_0^\infty (hDW - p) \left(\frac{3}{2}z^2 - \frac{1}{2} \right) r^4 dr, \quad (6)$$

where $D = \rho W$ is the conserved rest-mass density, W is the relativistic Lorentz factor, h is the relativistic enthalpy, p is the pressure, and $z = \cos \theta$. Expression (6) represents a slight modification of the Newtonian standard quadrupole formula (SQF₁) and it was shown to provide the best agreement with the gauge-invariant waveforms when compared with alternative definitions [18].

IV. RESULTS

A. Effects of the gravitational potential

As mentioned in the Introduction, for a certain set of initial conditions the ringdown phase of the gravitational-wave signal from a perturbed black hole shows the presence of the first QNMs of the black hole (typically, the fundamental mode and the first overtone) together with “backscattering” or “tail” effects. While the less damped modes are related to the interaction of the perturbations with the peak of the black hole Regge-Wheeler potential, the tail-effect cannot be associated to QNMs and are instead due to the long-range features of the potential and in particular to its slow decay with radius.

In order to single out the contribution of the peak of the curvature potential on the generation of the resulting gravitational-wave spectrum, while suppressing the effect of the tail term, we solve a simplified version of Eq. (2) in which the Regge-Wheeler potential is replaced by the so-called Pöschl-Teller potential [40, 41], which is exponentially decaying for $r_* \rightarrow \pm\infty$. We therefore evolve in time an equation of the type

$$\partial_t^2 \Psi_\ell - \partial_{r_*}^2 \Psi_\ell + U_\ell \Psi_\ell = 0, \quad (7)$$

where U_ℓ is given by

$$U_\ell \equiv \frac{V_\ell^{\max}}{\cosh^2 [\alpha(r_* - r_*^{\max})]} \quad (8)$$

and r_*^{\max} is the position of the peak of the Regge-Wheeler potential $V_\ell^{\max} \equiv V_\ell^{(o)}(r_*^{\max})$ and α is determined through the matching of the second derivatives at r_*^{\max} ; i.e., $d^2 U_\ell / dr_*^2 = d^2 V_\ell^{(o)} / dr_*^2$ at $r_* = r_*^{\max}$. In the following, for simplicity we will consider only the $\ell = 2$ odd-parity perturbations.

The Pöschl-Teller potential is shown in the top left panel of Fig. 1 together with $V_2^{(o)}$. Although the exponential decay of the former is evident for large r_* , it is also apparent that it provides a good approximation to the Regge-Wheeler potential near the peak. The accuracy of the approximation was first studied in Ref. [42], where it was pointed out that the QNMs of the Pöschl-Teller potential can be computed analytically. The frequencies found for the lower modes agree within a few percent with those obtained using the true curvature potential $V_\ell^{(o)}$, computed numerically in [43].

We solve Eq. (7) using a Lax-Wendroff method on an evenly spaced r_* grid with $\Delta r_* = 0.1 M$ and with initial data given by a Gaussian pulse $\Psi_2 = N \exp[-(r - r_c)^2 / \sigma^2]$ where r_c is the initial position of the pulse and N a normalization constant. The initial pulse is considered to be purely ingoing (i.e., with $\partial_t \Psi_2 = \partial_{r_*} \Psi_2$). We compare the signal extracted at $r_{\text{obs}} = 200 M$ for different values of σ using either the Regge-Wheeler or the Pöschl-Teller potential. This is summarized in Fig. 1, which shows the waveforms obtained for different values of r_c and σ and expressed in the retarded time, $u = t - r_*^{\text{obs}}$. Note that the waveforms from the Pöschl-Teller have been shifted in time so as to overlap the maxima and the minima of the ringdown phase of the Regge-Wheeler potential. This is necessary because the scattering of the pulse starts earlier for the Regge-Wheeler potential than for the Pöschl-Teller one.

Let us focus first on the top right panel of Fig. 1, which refers to a very narrow pulse ($\sigma = M$) initially located at $r_c = 100 M$ and shows with a solid and a dashed line the waveforms obtained with the Regge-Wheeler and Pöschl-Teller potentials, respectively. Clearly, the ringing is very similar in the two cases both in the wavelength and in the amplitude, but differences become apparent after $u/M \simeq 180$, when the tail term of the Regge-Wheeler potential becomes dominant and the gravitational-wave signal is driven by the backscatter due to the r^{-2} decay and asymptotes the expected late-time decay according to Price’s law [44]. Since the Pöschl-Teller potential decays exponentially, no tail effects are found and the signal is still given by a superposition of exponentially damped harmonic oscillations. Smaller differences between the waveforms are however present also in the early part of the waveform (cf., the inset of the top right panel of Fig. 1) and are, again, due to the fact that the interaction of the perturbation with the Regge-Wheeler potential starts “earlier” (i.e., at larger radii) than in the case of the Pöschl-Teller potential.

The two bottom panels of Fig. 1 refer instead to a wavepacket that is initially closer to the black hole (i.e., $r_c = 50 M$) and show the impact on the waveforms of an increasing width of the wave-packet. Most notably, the two panels show that as σ is progressively increased, the effects due to the slow-decay of the Regge-Wheeler potential become progressively more pronounced, with the ringdown lasting progres-

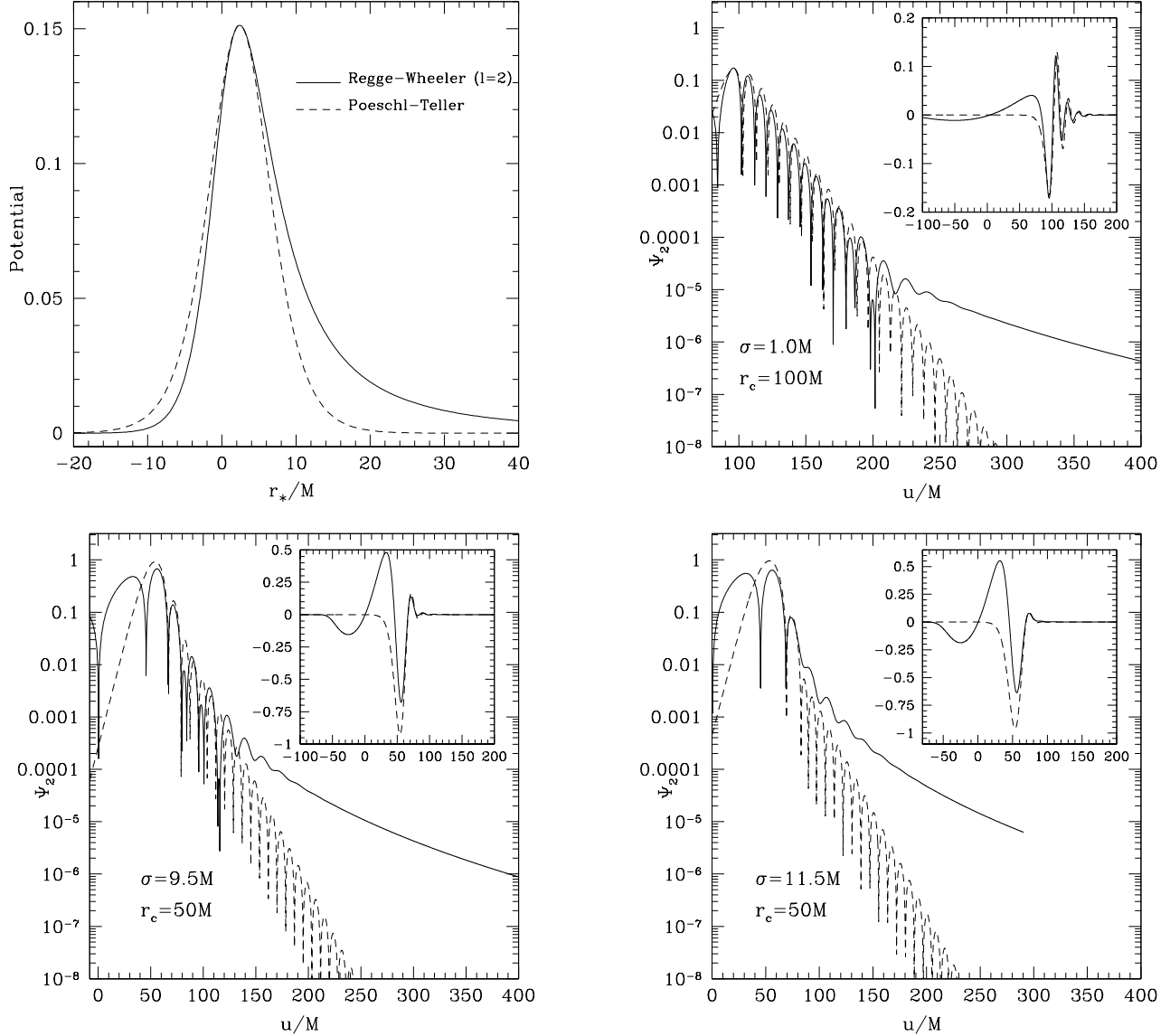


Figure 1: Comparison between the outcome of a scattering problem over the Regge-Wheeler (solid lines) and the Pöschl-Teller (dashed lines) potential. The waveforms are extracted at $r_{\text{obs}} = 200 M$ and refer to a choice of the parameters given by (from top to bottom and from left to right): $\sigma = M$ and $r_c = 100 M$, $\sigma = 9.5 M$ and $\sigma = 11.5 M$ with $r_c = 50 M$. The wider the pulse, the larger the differences between the two solutions. The top left panel shows a comparison between the profiles of the Regge-Wheeler and the Pöschl-Teller potentials.

sively less and with the backscattering being correspondingly anticipated. For example, when $\sigma = 9.5 M$ (left-bottom panel of Fig. 1) and despite the fundamental mode is still recognizable, other oscillations are present already after $u/M \sim 70$, while for $\sigma = 11.5 M$ (right-bottom panel) the global waveform is essentially overwhelmed by backscattering, the QNMs are almost absent and the signal is dominated by the “tail”. An additional increase in the pulse width would make the QNMs disappear completely. Clearly, this behavior is not present in the case of a scattering off a Pöschl-Teller potential, which is much less sensitive to the finite-size of the perturbation as long as it is smaller than the scale-height set by the exponential decay.

Although just a toy-problem, this simple comparison of the

black-hole response when modeled with the Pöschl-Teller potential is very useful to clarify that in the case of general initial data with a finite size, the shape of the curvature potential strongly affects the gravitational waveform. In the next sections we will refine this finding by considering more realistic perturbations such as those produced by the accretion of extended distributions of matter.

B. Quadrupolar shells of dust

Following the analysis presented in Paper I, we here consider a number of aspects of gravitational-wave emission resulting from the accretion of quadrupolar shells of dust which

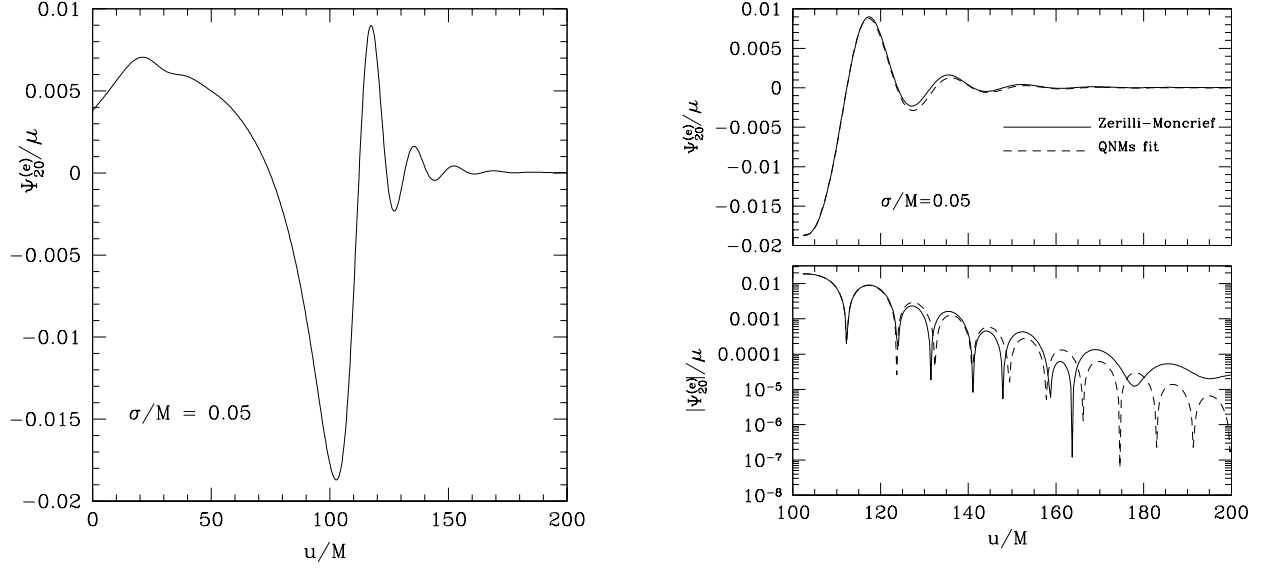


Figure 2: The $\ell = 2$ gravitational Zerilli-Moncrief function extracted at $r_{\text{obs}} = 500 M$ for a dust shell falling from $r_0 = 15 M$ with $\sigma/M = 0.050$. *Left panel:* the complete waveform. *Right panel:* investigation of the presence of the black hole QNMs: the dashed line was obtained through a non-linear fit with the first five modes and the comparison with the computed waveform is shown on both a linear and a logarithmic vertical scale.

were not investigated in detail before. More specifically, we will here discuss: *i*) a more detailed analysis of the black hole ringdown phase, focusing on black hole QNMs and on backscattering effects related to the non-exponential decay of the black hole potential; *ii*) the mechanism responsible for the production of the interference fringes in the energy spectra; *iii*) the effect of using conformally-flat initial data; *iv*) a more detailed analysis of the energy released in gravitational waves.

As in Paper I, the rest-mass density is parameterized as

$$\rho = \bar{\rho} + \rho_0 \exp[-(r - r_0)^2/\sigma^2] \sin^2 \vartheta, \quad (9)$$

where r_0 is the initial position of the “center” of the shell and σ controls its compactness. The background rest-mass density $\bar{\rho}$ is chosen to be very small (i.e., $\sim 10^{-22}$) to simulate the vacuum outside the black hole, while the normalization constant ρ_0 is obtained from the condition that the volume integral of Eq. (9) gives μ , the total mass of the shell, which we choose to be $\mu = 0.01 M$. As we mentioned in Sec. II B (and Paper I), the initial profile for $\Psi_{20}^{(e)}$ is obtained after solving the Hamiltonian constraint for k_{20} with $\beta = 0$. Furthermore, to minimize the impact of spurious radiation and produce initial data that is a “almost” time-symmetric, the shell is kept frozen at r_0 (i.e., the hydrodynamics equations are not evolved) up until the spurious initial gravitational-wave pulse leaves the numerical grid. We shall show at the end of this Section how waveforms and energy spectra change when “genuine” time-symmetric and conformally flat initial data are implemented.

We start by considering the plunge from $r_0 = 15 M$ with $\sigma/M = 0.050$ (this particular model was discussed also in Paper I) and whose complete waveform is shown in the left panel of Fig. 2. As expected, the gravitational-wave signal contains signatures of both the black hole QNMs and of the backscattering effects. The first ones are triggered

when the maximum of the rest-mass density crosses the peak of the potential at $r \sim 3 M$ yielding the largest contribution to the waveform at $u/M \simeq 112$. We have verified the presence of the black hole QNMs with complex frequency ω_i (with $i = 1, 2, \dots$) by fitting the waveform from this time onward with a superposition of modes of the form $\Psi^{(e)} = \sum_i [\alpha_i \cos(\Re(\omega_i)t) + \beta_i \sin(\Re(\omega_i)t)] \exp[\Im(\omega_i)t]$, where the free coefficients α_i and β_i are real. The right panel of Fig. 2 reports the result of such fit obtained using the first five QNMs, and which is essential to properly capture the early-time part of the waveform. (Adding higher modes does not improve the fit, while considering less modes is not enough to reproduce accurately the waveform.) When analyzed on a logarithmic scale (see bottom part of the right panel of Fig. 2), it becomes evident that after $u/M \sim 130$ the backscattering effects become dominant and the waveform is no longer a simple superposition of exponentially decaying modes.

Additional information on the black hole response comes from the study of the energy spectra for shells of different initial width σ and starting from $r_0 = 15 M$. This is summarized in Fig. 3, whose left panel shows the energy spectra of the complete waveforms and the characteristic interference patterns already introduced in Paper I. Clearly, the interference effects at higher frequencies (i.e., for $2M\omega \gtrsim 0.2$) as well as the efficiency in the emission of energy via gravitational waves are increased as the compactness of the shell is increased, progressively tending to what is expected for a point like particle (cf. the top-right panel in Fig. 4). Equally clear is that the energy spectra do not show any peculiar behavior around the QNMs frequencies (i.e., for $2M\omega \gtrsim 0.35$) but also that the behavior of the spectra at low frequencies does not change significantly with the matter compactness.

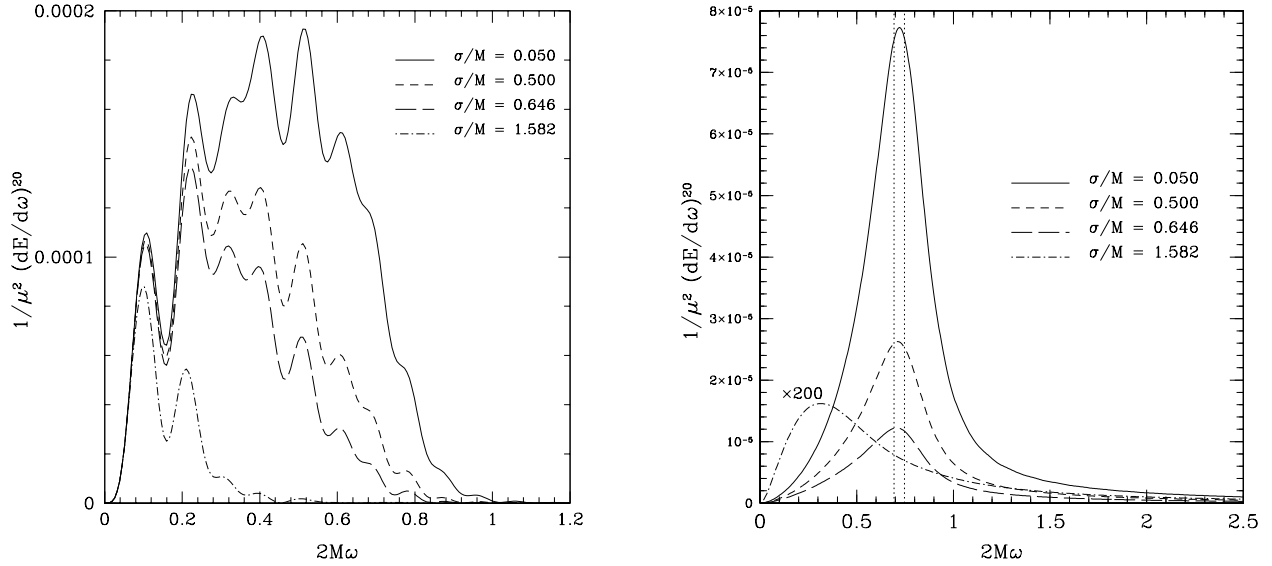


Figure 3: *Left panel:* Energy spectra and their typical interference fringes as computed from the waveforms produced by shells infalling from $r_0 = 15M$. *Right panel:* The same as in the left panel but only for the ringdown phase, showing the excitation of the $\ell = 2$ black hole QNMs. See text for details.

As argued in Paper I and in Refs. [8, 23], interference fringes naturally arise in the energy spectrum generated by the superposition of two waveforms separated by a certain time lag T . Indeed, given two time series $A_1(t)$ and $A_2(t) = CA_1(t + T)$, the power spectral density resulting from their superposition is given by

$$\frac{dE}{d\omega} \propto |\tilde{A}_1(\omega)|^2 [1 + C^2 + 2C \cos(\omega T)] , \quad (10)$$

where $\tilde{A}_1(\omega)$ is the Fourier transform of $A_1(t)$. As a result, such a spectral density will have peaks with a constant spacing given by $\Delta\omega = 2\pi/T$. If $C = 1$, the minima occur at $dE/d\omega = 0$ and the spectrum is said to have 100% frequency modulations. The modulation is always smaller for generic values of C .

The energy spectra displayed in the left panel of Fig. 3 can be explained within this general picture. The series of fringes is mainly determined by the interference of two bursts of radiation with different amplitude and separated in time by the scattering off the curvature potential at different times. In the case of a shell of width $\sigma/M = 0.050$, the two main pulses responsible for this modulation can be distinguished in the waveform shown in the left panel of Fig. 2. These correspond to the peak produced by the initial motion of $\Psi_{20}^{(e)}$ and appearing at very early times (i.e., at $u/M \sim 20$), and to the one emitted when the bulk of accreting matter crosses the peak of the Zerilli potential (i.e., around $u/M \sim 112$). [48] The time-lag between the two pulses is $\Delta u/M \sim 92$, which gives a separation between the peaks of the spectrum $2M\Delta\omega \sim 0.07$. This value is in good agreement (given the difficulty in unambiguously catch the time when the ringdown starts) with the $2M\Delta\omega \sim 0.1$ that can be read off from the solid line in the left panel of Fig. 3.

The right panel of Fig. 3, on the other hand, shows the spectra obtained by performing a Fourier transform of the signal in the “ringdown” phase only. The two dotted vertical lines indicate the $n = 1$ (fundamental) and $n = 2$ (first overtone) QNM frequencies of the black hole. It is interesting to note that with the exception of very wide shells (i.e., with $\sigma/M = 1.582$) which are not able to excite cleanly the QNMs, the maximum of the spectra always lies between the two lines, suggesting the presence of the two modes in the waveform.

Another parameter influencing the energy spectra is the initial location of the shells r_0 . As mentioned above, the largest part of the gravitational-wave signal is emitted when the “center” of the shell reaches the peak of the Zerilli potential and this will clearly depend on the initial position of the shell. Shells that start further away will have longer infalling times, larger separations between the first and second peaks in the waveforms, and thus smaller separation in the interference fringes of the energy spectra.

In order to reproduce this dependence we have performed a number of simulations for shells of fixed initial width ($\sigma/M = 0.050$) accreting from different initial locations r_0 . Two representative and extreme cases for $r_0 = 10M$ and $r_0 = 70M$ are shown in Fig. 4, whose left panels display the waveforms, while the right ones the energy spectra. Overall, these plots show a number of interesting and general properties of the excitation of black hole oscillations through accreting matter. Firstly, as the infalling time is increased, the ringdown phase is progressively dominated by the non-oscillatory tail, essentially as a result of the “spreading” of the shell induced by the tidal field. This behavior is indeed consistent with the analysis carried out in Ref. [45] and which pointed out that the excitation of the black hole QNMs through a continuous flux of infalling particles is made difficult by the presence of destructive interferences effects.

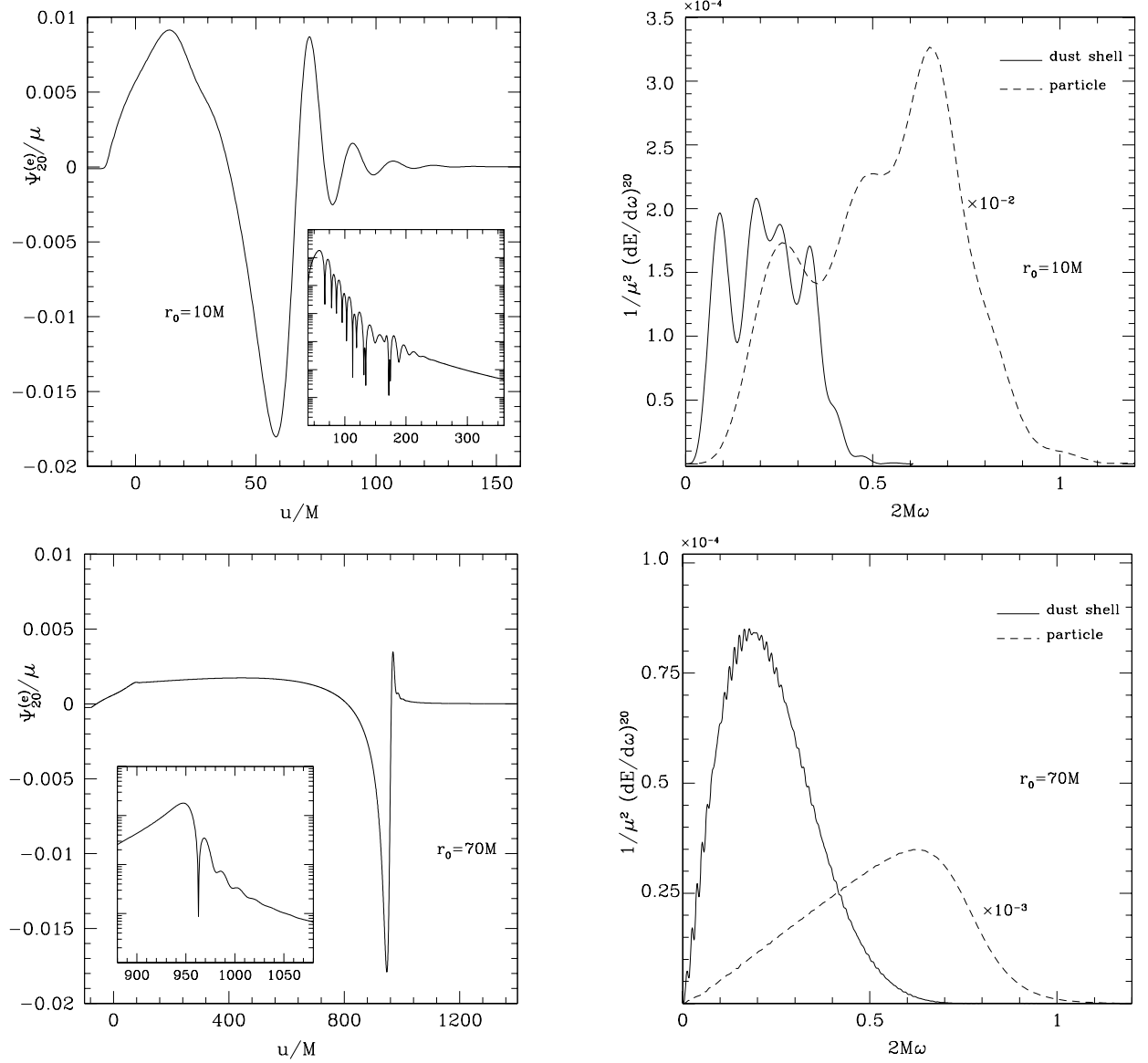


Figure 4: Infalling shells of dust: waveforms (*left panels*) and energy spectra (*right panels*) for two representative values of r_0 with $\sigma/M = 0.050$. For the sake of comparison, the right panels show in dashed lines the $\ell = 2$ energy spectra for a particle plunging radially onto the black hole (rescaled by a convenient factor).

Secondly, the efficiency in gravitational-wave emission decreases for shells falling from larger distances and is significantly smaller than for point-like particles. This can be easily appreciated in the right panels of Fig. 4, when comparing energy spectra associated with shells (solid lines) with the corresponding $\ell = 2$ energy spectra of a particle plunging radially from the same initial position (dashed line)[49]. Note that the efficiency is in this case of at least a couple of orders of magnitude larger (the data have been properly rescaled to aid the comparison).

Thirdly, the energy emission is progressively peaked toward lower frequencies as r_0 increases. This behavior can be made more quantitative by defining the “characteristic frequency”

of the energy spectrum as the weighted average

$$\omega_c \equiv \frac{\int \omega (dE^{20}/d\omega) d\omega}{\int (dE^{20}/d\omega) d\omega}, \quad (11)$$

and by computing how this characteristic frequency changes along a sequence of shells of fixed initial compactness and falling from increasingly larger radii. A summary of this dependence is offered in Fig. 5 for shells with $\sigma/M = 0.158$. By following a phenomenological approach, if one defines $x = \log_{10}(r_0/M)$ and $y = \log_{10}(2M\omega_c)$ the figure shows that the data can be very well fitted by means of a quadratic law like $y = ax^2 + bx + c$ with $a = -0.461$, $b = 1.002$ and $c = -0.904$. The interpretation of this relation is still unclear but certainly deserves further attention.

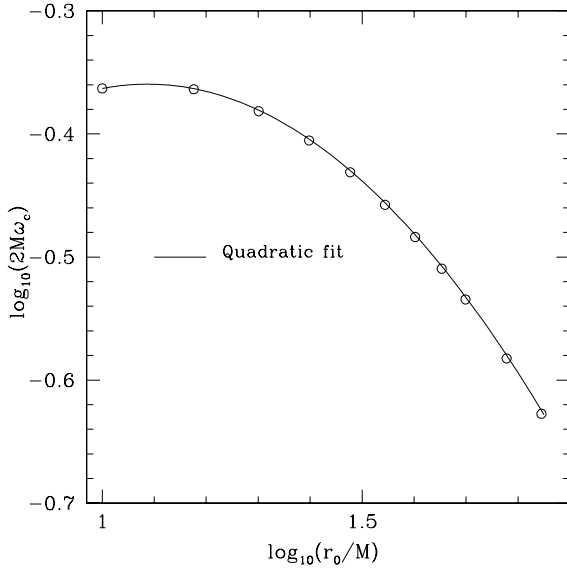


Figure 5: Dependence of the characteristic frequency in the energy spectrum on the initial position of the shell.

As we anticipated at the beginning of this section, an important comment is worth making on the influence of the initial amount of gravitational radiation on the waveforms and on the energy spectra. Two different approaches are possible in this respect and it is important to bear in mind that they do not yield identical results. The first one [50] consists in selecting a time-symmetric and conformally flat (or non-conformally flat) initial profile of the Zerilli-Moncrief function from the solution of Hamiltonian constraint. As we discussed in Sec. II B, this does not prevent that spurious radiation is produced as the evolution starts. The second approach, which has been the one adopted here, consists, after the solution of the constraint, in the removal of the spurious burst of gravitational radiation by evolving the perturbation equations but *not* the perturbing sources. In this way the initial radiation is allowed to leave the computational domain and the evolution can therefore start self-consistently once the initial, nonstationary part of the solution has been removed. Figure 6 summarizes the impact on the energy spectra and on the waveforms of the two approaches for a shell initially at rest at $r_0 = 7.5M$. Plotted with the dashed line in the main panel is the energy spectrum in the case of actual conformally flat initial data involving the solution of Hamiltonian constraint only; on the other hand, the solid line refers to the spectrum one obtains when the initial pulse is allowed to be radiated away. Note the much stronger modulation present in the former case and the corresponding larger variation in the initial part of the waveform as shown in the inset. Note that we would have found larger differences for smaller r_0 and smaller differences for larger r_0 . Furthermore, we note that if we start with non-conformally flat initial data (that is, through the solution of Hamiltonian constraint with $\beta \neq 0$) we would obtain larger differences in the early part of the waveforms and thus larger modulations in the energy spectrum. This behavior is qualitatively similar to what discussed in Ref. [23] in the case of particles plunging radially

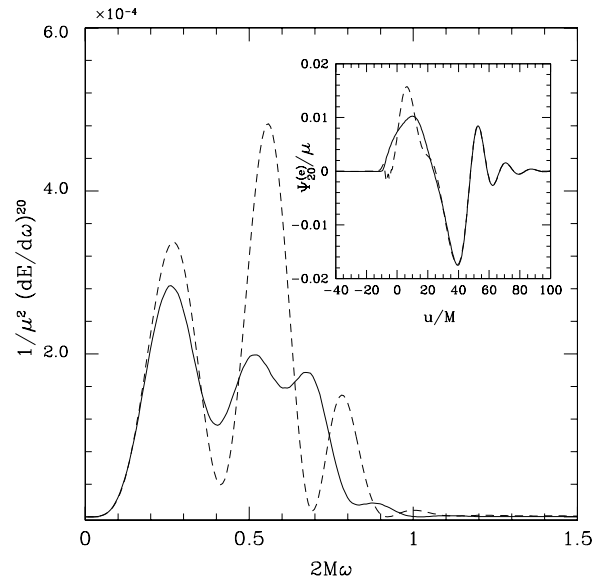


Figure 6: Conformally flat initial data and spurious bursts of radiation: energy spectra obtained by solving the Hamiltonian constraint with $\beta = 0$ only (dashed line) and when the initial gravitational-wave pulse is additionally eliminated (solid line). The shell has $\sigma/M = 0.158$, it falls from $r_0 = 7.5M$ and the signal is extracted at $r_{\text{obs}} = 500M$. The inset shows the corresponding initial part of the waveform.

from finite distance

We conclude this section by commenting on the amount of energy released in gravitational waves as a function of both r_0 and σ . This is shown in Fig. 7, which displays in the main panel the normalized energy emitted in the lowest multipole as a function of the initial location r_0 and for a shell of initial width $\sigma/M = 0.158$. Note that in the case of a shell this is a monotonically decreasing function of the radial distance, an opposite behavior to that seen for accreting particles where, for conformally flat initial data, the energy has a local minimum and then increases monotonically with r_0 [8], asymptoting the Davis-Ruffini-Press-Price limit [47]. In addition, the inset in Fig. 7 displays a comparison between the energy emitted through the whole waveform (empty circles) and the one computed considering the ringdown phase only (filled circles). Note that while the black hole ringdown contributes for $\sim 30\% - 40\%$ of the total energy in the case of small r_0 , this value goes down to $\sim 10\%$ for larger initial distances as a result of the progressive loss of compactness experienced by the shell during the infall.

C. Thick accretion disks

While our model with infalling quadrupolar shells allows us to capture some of the essential features of the gravitational-wave emission from extended matter sources, such as the excitation of the black hole QNM ringdown and the presence of interference effects in the energy spectra, it nevertheless remains a useful toy model.

Table I: Stable (D_0 and D_1) and marginally stable (D_2) constant angular momentum thick disks orbiting around a Schwarzschild black hole of mass $M = 2.5M_\odot$. From left to right, the columns report the name of the model, the number of radial and polar gridzones used in the hydrodynamical simulations, the disk-to-hole mass ratio, the polytropic constant κ of the isentropic EOS $p = k\rho^\gamma$ with $\gamma = 4/3$, the value of the specific angular momentum l , the position of the cusp r_{cusp} and of the center r_{center} of the disk, the rest-mass density at the center ρ_c , the location of the inner (r_{in}) and outer (r_{out}) disk boundaries, the value of the potential barrier ΔW , and the orbital period at the center t_{orb} .

Model	N_r	N_θ	μ/M	κ (cgs)	l	r_{cusp}	r_{center}	ρ_c (cgs)	r_{in}	r_{out}	ΔW	t_{orb} (ms)
D_0	300	150	0.0077	2.25×10^{13}	3.72	5.06	7.27	7.31×10^{12}	5.26	9.50	-1×10^{-4}	1.51
D_1	300	150	0.0463	9.00×10^{13}	3.80	4.57	8.35	6.86×10^{12}	5.21	14.54	-0.002	1.87
D_2	300	150	0.0779	1.05×10^{14}	3.80	4.57	8.35	8.74×10^{12}	4.57	15.89	0	1.87

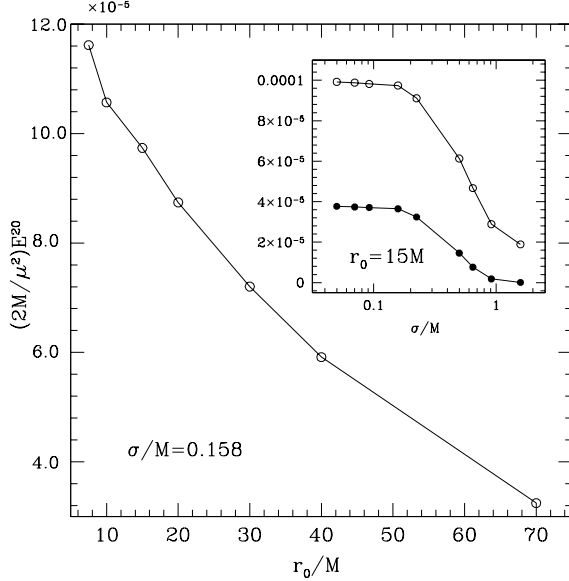


Figure 7: *Main panel:* Total energy radiated in gravitational waves ($l = 2$ multipole) as a function of the initial location r_0 of the center of a shell with $\sigma/M = 0.158$. *Inset:* Total energy versus σ for shells falling from $r_0 = 15M$ (open circles). The filled circles refer to the energy contribution coming from the black hole ringdown only.

To improve on this and to examine a scenario which is astrophysically more realistic, we will now consider the gravitational-wave emission resulting from the accretion of geometrically thick disks (or tori) orbiting around a non-rotating black hole. Such systems are believed to form in a variety of different ways, such as during the last stages of gravitational collapse or in the merger of binary neutron stars. In addition, if compact enough and undergoing oscillations, these systems generate gravitational-wave signals within the sensitivity curve of ground-based interferometers [18, 26, 27]. Hereafter, and as in the case of dust shells, we will assume that the mass of the torus μ is much smaller than that of the black hole.

Detailed descriptions on how to build equilibrium configurations of barotropic thick disks orbiting black holes are given in Refs. [24, 25], but we here recall that these objects have traditionally been described as obeying a polytropic equation of state $p = \kappa\rho^\gamma$, with $\gamma = 4/3$. Because in pure orbital motion, the fluid four-velocity is given by $u^\alpha = (u^t, 0, 0, u^\phi)$

and it describes a non-Keplerian rotation around the central black hole, with a specific angular momentum $\ell = -u_\phi/u_t$ distribution which is essentially unknown.

Table I lists the main features of the tori considered in our simulations, such as the values of the specific angular momentum ℓ (assumed constant throughout the disk), of the potential gap ΔW between the inner edge of the disk and the cusp, and of the mass of the disk μ . In order to induce a non-trivial dynamics in these otherwise stationary disks, the initial models have to be perturbed in some way, such as by adding a radial velocity $v_r = \eta v_r^{\text{sph}}$, where η is a parameter and v_r^{sph} is the radial velocity of the spherical stationary atmosphere surrounding the torus [26]. The rest-mass density of the atmosphere is low enough not to influence the dynamics of the tori (its density is several orders of magnitude smaller than the maximum density at the center of the disk).

As in the case of infalling dust shells, the initial data for the perturbation fields $\Psi_{\ell 0}^{(e/o)}$ is obtained either through the solution of the Hamiltonian constraint (for even-parity perturbations) with conformally flat initial data, or assuming stationarity, i.e., through Eqs. (2) with $\partial_t^2 \Psi_{\ell 0}^{(e/o)} = 0$. Clearly, in either case this initial data is not consistent with the hydrodynamical sources once they are perturbed. This mismatch inevitably introduces an unphysical initial burst of gravitational radiation that is however easy to distinguish and remove from the analysis.

We note that the accretion of matter onto the black hole can occur on different timescales depending on the perturbation and we will consider here the two limiting situations that could be encountered in astrophysical scenarios. In the first case we will consider a perturbation which is large enough to cause a runaway accretion of the disk onto the black hole; we will refer to this as the “hypercritical accretion” scenario (see Sect. IV C 1). In the second case, on the other hand, the perturbation is smaller and it will induce a series of quasi-periodic oscillations, each accompanied by an episode of accretion onto the black hole; we will refer to this as to the “quasi-period accretion” scenario (see Sect. IV C 2).

1. Hypercritical Accretion

As mentioned above, simulations of hyper-accreting disks can be performed by simply choosing a sufficiently large initial value of the radial velocity perturbation. Under this con-

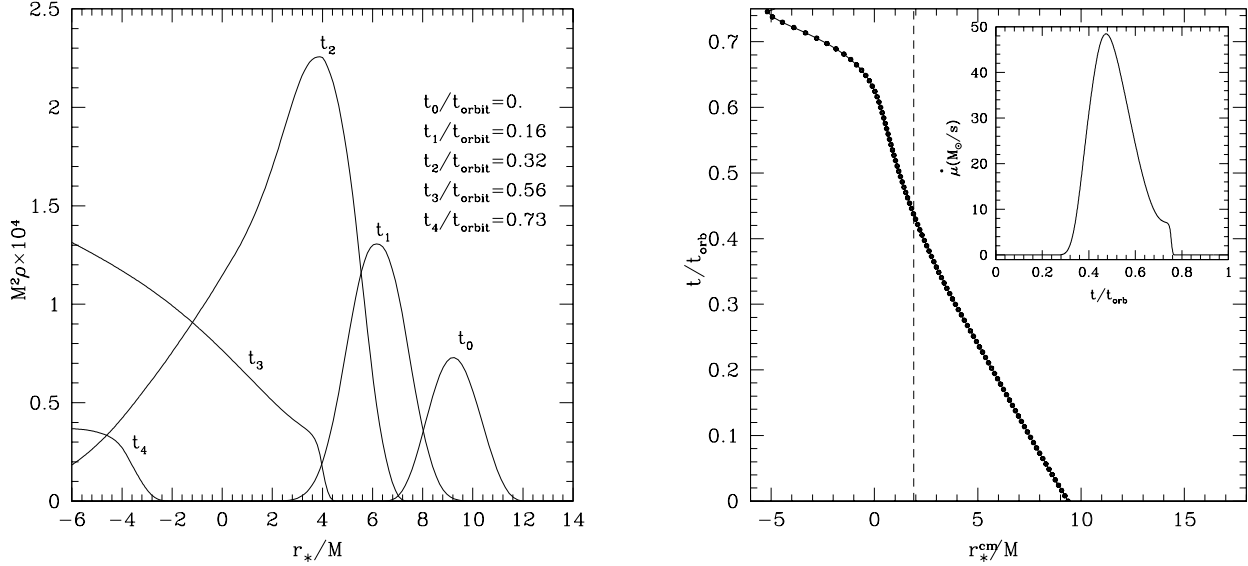


Figure 8: Model D_0 . *Left panel*: time evolution of the equatorial rest mass density profiles for a velocity perturbation $\eta = 0.3$. *Right panel*: time evolution of the center of mass in the equatorial plane. The disk disappears in the black hole at $t \approx 0.75 t_{\text{orb}}$.

dition, the centrifugal barrier cannot counteract the injection of additional kinetic energy and the whole disk is “pushed” towards the black hole, rapidly accreting onto it in less than one orbital period.

Hereafter we will concentrate on the dynamics of model D_0 , to which a velocity perturbation with $\eta = 0.3$ is added. For this model the hydrodynamical grid runs from $r_{\text{min}} = 2.03 M$ to $r_{\text{max}} = 16 M$ and it is covered by 300×150 grid-points, geometrically spaced in the coordinate r , with $\Delta r_{\text{min}} = 3 \times 10^{-4}$ and $\Delta r_{\text{max}} = 0.2$. The range of the r_* 1D grid is $r_* \in [-2200 M, 4500 M]$, to guarantee that the outer boundary does not influence the slope of the late time power-law tail, and is covered by $\sim 3 \times 10^4$ cells.

The left panel of Fig. 8 shows, in terms of the tortoise coordinate, five snapshots of the evolution of the rest-mass density on the equatorial plane. Note that as time proceeds, the disk is compressed, the density increases and matter quickly starts falling onto the black hole. This continues until the entire disk has been accreted. A summary of this is shown in the space-time diagram in the right panel of Fig. 8, which presents the motion of the projection on the equatorial plane of an effective “center-of-mass” of the disk, defined as

$$r_{\text{cm}} \equiv \frac{\int \sqrt{g_{rr}} \rho r^2 dr}{\int \sqrt{g_{rr}} \rho r dr}, \quad (12)$$

where $g_{rr} = (1 - 2M/r)^{-1}$ (for convenience the spacetime diagram is shown using the tortoise radial coordinate r_*). Correspondingly, the inset in Fig. 8 depicts the time evolution of the mass accretion rate for model D_0 .

The vertical dashed line in the right panel of Fig. 8 is approximately the location of the peak of the Zerilli potential, $r_*^{\text{peak}} \simeq 1.90 M$ ($r^{\text{peak}} \simeq 3.1 M$) and can be used to identify $t \simeq 0.44 t_{\text{orb}}$ as the time at which the center of mass crosses the peak of the potential. Furthermore, this panel

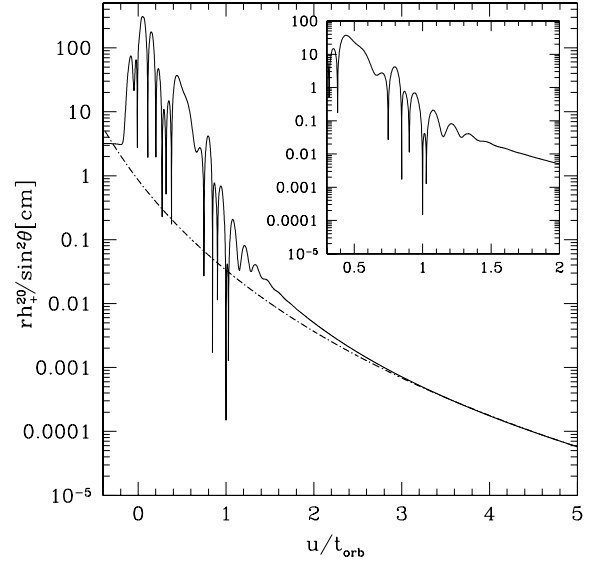


Figure 9: Model D_0 : gravitational waveform (extracted at $r_{\text{obs}} = 200 M$). The presence of two ringings is evident. The first one is related to the gravitational-wave content present in the initial profile of the Zerilli-Moncrief equation. The second ringing (magnified in the inset) is determined by the object crossing the peak of the potential. The dashed line, proportional to u^{-7} , shows that the late-time behavior of the waveform is properly captured.

also shows that the center of mass leaves the hydrodynamical grid ($r_*^{\text{min}} \simeq -6.35 M$) at $t \sim 0.75 t_{\text{orb}}$ and from this time onward, the gravitational-wave signal is dominated by the QNMs of the black hole.

The gauge-invariant gravitational waveform produced by the hypercritical accretion has a dominant $l = 2$ character[51] and is displayed in a logarithmic scale in Fig. 9 as measured

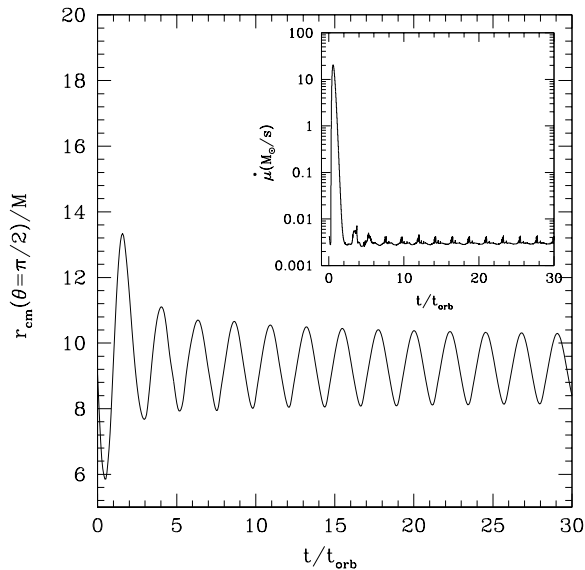


Figure 10: Model D_1 : time evolution of the projection of the center of mass in the equatorial plane. After an initial transient, the dynamics is characterized by constant amplitude quasi-periodic oscillations. The inset shows the mass accretion rate.

by an observer located at $r_{\text{obs}} = 200 M$. Besides the initial burst of spurious radiation related to the initial data, and which is no longer present by $u \simeq 0.2 t_{\text{orb}}$, the waveforms exhibit two main features. The first one is determined by the infalling matter as its center of mass approaches the maximum of the potential at $u \simeq 0.4 t_{\text{orb}}$. The second one, instead, starts at $u \simeq 0.7 t_{\text{orb}}$ and represents the ringing resulting from the perturbation experienced by the black hole through the rapid accretion of the torus (see the mass accretion rate inset in the right panel of Fig. 8). This becomes apparent when comparing the features of the waveform in Fig. 9 with the matter dynamics in Fig. 8. The ringdown phase ends with the usual power-law tail; this is highlighted by the dot-dashed line in Fig. 9 which is proportional to u^{-7} and shows that for $u > 3.6 t_{\text{orb}}$ the waveform has only a quadrupolar nature decaying as $\propto u^{-(2\ell+3)}$.

In summary, the analysis of the process shows that a very rapid and hypercritical accretion of a compact distribution of matter onto a black hole produces gravitational-wave emission that is qualitatively similar to that of either relatively narrow dust shells plunging from a large distance or wide dust shells accreting from a small distance. Furthermore, the gravitational-wave signal shows oscillations that reflect the excitation of the black hole QNMs (especially the fundamental one) but these oscillations are in general so weak that the non-oscillatory tail determined by the long-range properties of the scattering potential soon dominates the signal.

2. Quasi-periodic accretion

A phenomenology complementary to the one discussed in the previous section for a hypercritical accretion can be stud-

ied when the accretion takes place in a quasi-period fashion. Indeed, there are at least two different ways of triggering a quasi-periodic accretion and we will discuss them separately.

The first possibility has already been discussed in Sect. IV C and consists in adding a perturbation in the radial velocity of the torus parameterized in terms of an analytic accretion solution. As a concrete example we will now concentrate on the dynamics of model D_1 , describing a disk with a comparatively high value of the specific angular momentum, $l = 3.80$, and subject to an initial radial velocity perturbation with $\eta = 0.2$.

Figure 10 shows the motion of the center of mass on the equatorial plane, indicating that after an initial transient, a phase of quasi-periodic, (almost) constant amplitude oscillations follows, in which the disk periodically approaches the black hole before the centrifugal barrier pushes it back, past its original position. As the torus nears the black hole, part of its matter is spilled through the cusp, resulting in a quasi-periodic accretion of matter onto the black hole; this is shown by the inset of Fig. 10 which reports the evolution of the mass accretion rate (see Ref. [26] for a more detailed discussion). Note that the accretion is essentially shut-off as the torus moves away from the black hole.

This quasi-periodic dynamics of the torus is clearly imprinted onto the gravitational-wave signal and this is shown in the left panel of Fig. 11, where the $l = 2$ gauge-invariant waveform (extracted at $r_{\text{obs}} = 500 M$) is superposed to the signal extracted using the quadrupole formula (SQF₁). Note that the very early time part of the gauge-invariant signal has been removed to avoid influences coming from the burst related to the initial data. The waveforms show a small burst at $u \approx t_{\text{orb}}$, that corresponds to the initial accretion of matter, followed by regular oscillations that mirror the motion of the torus in the potential well. Some differences between the gauge-invariant and the SQF₁ waveforms are recognizable in the initial stages, with the first one showing highly damped high-frequency oscillations for $u \approx 2 t_{\text{orb}}$ superposed to the main, quasi-periodic signal. Since this high-frequency pattern is absent in the quadrupole waveform, we conclude that it originates from curvature backscattering of gravitational waves emitted in the initial infalling phase.

We also note that the differences between the waveforms computed through the gauge-invariant formalism and the quadrupole formula using the quadrupole tensor defined by Eq. (6) become larger if the initial velocity perturbation is increased. This is simply due to the fact that the SQF₁ is valid in the weak-field and slow-motion approximation and thus ceases to be accurate when the dynamics of the oscillations is nonlinear, with the velocities becoming relativistic. On the other hand, the velocity-dependent terms in the source function of the Zerilli-Moncrief equation are obviously accurate also in a relativistic regime.

The energy spectrum for this signal is shown as a solid line in the right panel of Fig. 11 and refers to the signal from $u/t_{\text{orb}} \gtrsim 1$ in order to eliminate the unphysical initial burst. The spectrum shows the presence of a broad-band peak at low frequencies, related to the highly damped oscillation in the early time part of the $l = 2$ signal, together with nar-

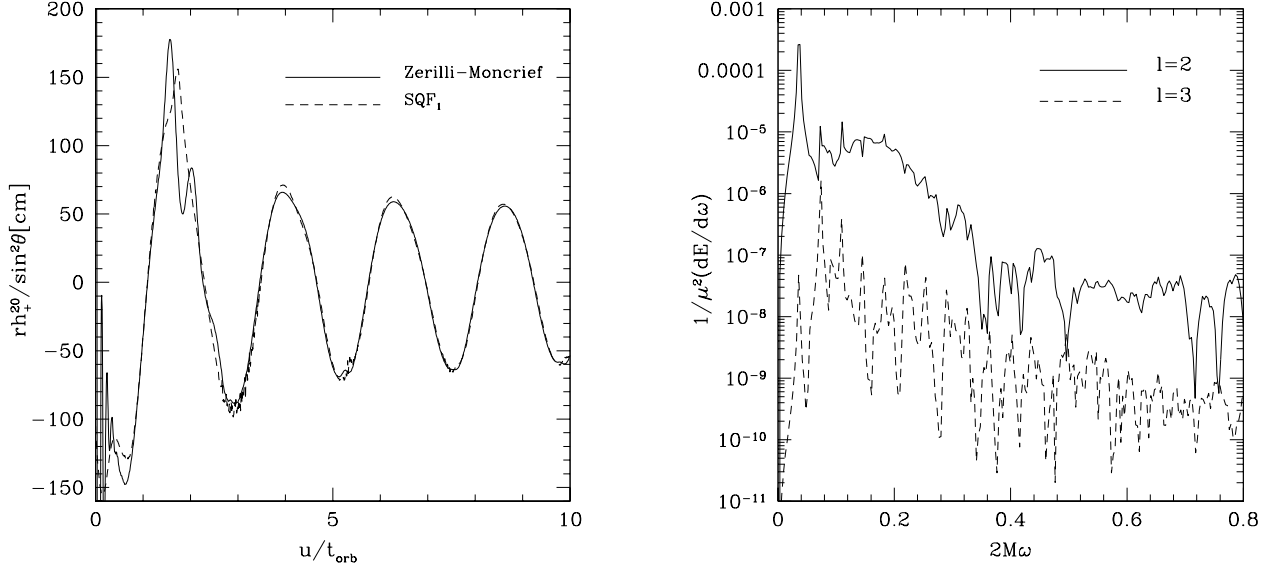


Figure 11: Model D_1 . *Left panel*: gravitational waveforms (extracted at $r_{\text{obs}} = 500 M$) versus retarded time. h_+^{20} polarization (even-parity) superposed to the waveform extracted using the SQF₁ (dashed line). *Right panel*: Energy spectrum for the $l = 2$ and $l = 3$ (odd-parity) modes. The highly damped oscillation in the early part of the $l = 2$ waveform (from $\Psi_{20}^{(e)}$) results in a broad-band peak which is not related to the QNMs frequencies of the black hole.

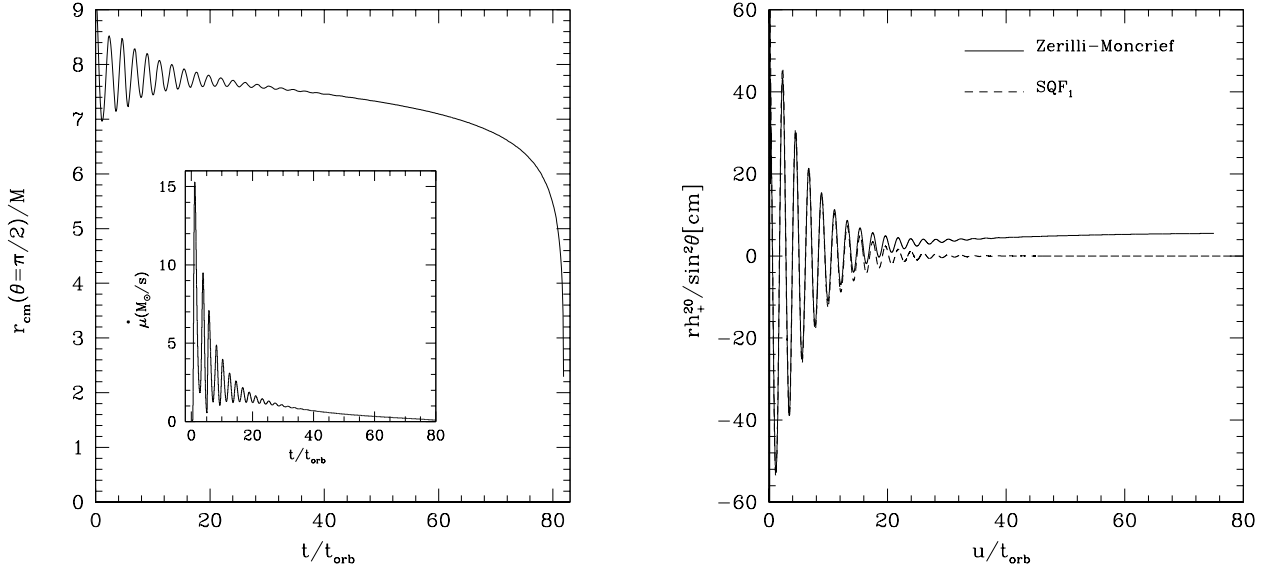


Figure 12: Model D_2 . *Left panel*: the motion of the center of mass on the equatorial plane and the mass accretion rate (in the inset). *Right panel*: the quadrupole gravitational waveforms. The gauge-invariant (extracted at $r_{\text{obs}} = 500 M$) and the SQF₁ waveforms are shown on the same plot for comparison.

row peaks in the harmonic ratio $1 : 2 : 3 : \dots$, which instead mirror the non-linear coupling of modes in an oscillating torus (see Refs. [28, 29] for a detailed discussion of the eigenfrequencies and their astrophysical implications). Such peaks are present in both the $l = 2$ and $l = 3$ energy spectra (dashed line in Fig. 11). The latter is generated by a waveform $rh_\times^{30}/(\cos\theta\sin^2\theta)$ whose amplitude is roughly two orders of magnitude smaller than the $l = 2$ one. It is interesting to note that while for the $l = 2$ multipole the first frequency of

the disk is the dominant one, the second frequency has the largest power for the $l = 3$ multipole. The energy spectrum shows no distinctive signature at $2M\omega \simeq 0.7473$ that could be related with the excitation of the QNMs of the black hole (cf., right panel of Fig. 3). This is in contrast with the results of Ref. [19], which have simulated a similar source of perturbations for the black hole and have indeed found a minute high-frequency contribution in the energy spectra related to the emission from the black hole[52]. It is presently unclear

what is the origin of this difference, but it is likely that the hybrid approach proposed in Ref. [19], and which combines a solution in the time-domain for the hydrodynamics and one in the frequency-domain for the perturbative equations, is better suited to extract the extremely small contributions coming from the black hole.

A second possibility of triggering quasi-periodic oscillations in the disk, and hence a quasi-periodic accretion, is by an instantaneous reduction of the specific angular momentum. The main difference with the dynamics discussed before is that this reduction produces a continuous mass accretion, which is however modulated quasi-periodically as the torus approaches or moves away from the black hole. This behavior is shown in Fig. 12 for model D_2 , in which the specific angular momentum is reduced from $l = 3.80$ to $l = 3.72$. More specifically, the left panel of Fig. 12 shows the motion of the center of mass on the equatorial plane and the evolution of the mass-accretion rate in the inset. Because of the intrinsic reduction of the centrifugal support and the resulting continuous accretion, the oscillations are quasi-periodic in time but with decaying amplitude, so that by $t/t_{\text{orb}} \sim 50$ they have essentially disappeared and the torus accretes at an almost constant rate, with the center of mass progressively approaching the black hole.

This different quasi-periodic dynamics of the torus is also imprinted onto the quadrupolar waveform and this is shown in the right panel of Fig. 12, which presents both the gauge-invariant signal as measured by an observer located at $r_{\text{obs}} = 500 M$ (solid line) and the one computed with the SQF_1 (dashed line). Note that the differences between the signals are very small initially, but they grow with time and by $t \gtrsim 15t_{\text{orb}}$, when the angular momentum loss induces a global radial motion of the disk, the mean value of the gauge-invariant signal progressively drifts away from zero. This different behavior can be understood simply if one bears in mind that during this stage the disk is undergoing an almost steady-accretion phase. As a result, while the disks mass-quadrupole is nonzero and large, its time variations, and hence the corresponding gravitational-wave signal as computed in the SQF_1 , are essentially zero. The perturbative approach, on the other hand, is able to capture the perturbations induced by this steady-state accretion and this is reflected in the gradual and secular increase of the gravitational-wave signal shown in the right panel of Fig. 12. Of course, this behavior is the same already encountered in the case of accretion of dust shells and it is, once again, generated by curvature backscattering off the “tail” of the potential.

Note that during the final stages of the accretion, i.e., for $t \gtrsim 60 t_{\text{orb}}$, the motion of the center of mass exhibits an exponentially rapid motion toward the black hole which, however, is not reflected neither in the mass-accretion rate, nor in the gravitational-wave signal. The reason for this is that, in practice, the rest-mass contained in the torus in these final stages is extremely small and the rest-mass density is so diluted that it becomes comparable to that of the atmosphere surrounding the torus. As a result, the effective perturbation induced onto the black hole in the final stages of the accretion is vanishingly small.

In summary, the analysis of this process shows that the gravitational-wave signal produced by a quasi-periodic accretion can be rather different, depending on whether the amplitude of the oscillations is (almost) constant in time and the accretion rate is also periodic, or the oscillations have decreasing amplitude and the accretion rate is constant with a periodic modulation. In the first case, the gravitational-wave signal will reflect faithfully the dynamics of the matter with constant-amplitude waveforms averaging to zero and a spectrum showing peaks at the eigenfrequencies of the oscillating matter. In the second case, on the other hand, the waveforms will have a decreasing amplitude and will not average to zero as a result of the underlying continuous accretion.

V. CONCLUSIONS

By performing numerical simulations that combine the solution of the nonlinear hydrodynamics equations with that of the linear inhomogeneous Zerilli-Moncrief and Regge-Wheeler equations, we have studied the features of the gravitational-wave signals generated by the accretion of matter onto a Schwarzschild black hole.

As extended and accreting matter-sources we have considered quadrupolar shells of dust falling radially from a finite distance, as well as geometrically thick disks undergoing either bursts of hypercritical accretion or quasi-periodic oscillations. In both cases we find that the gravitational-wave signal *is not* a simple superposition of the black hole QNMs and that the latter cannot be found in the energy spectra at times. Rather, we find that quite generically the signal contains important contributions coming from radiation scattering off the tail of the curvature potential and producing a characteristic pattern of interference fringes in the energy spectra. While the relevance of this contribution differs according to the specific source considered, it is generically present as long as the source of perturbations is extended and the scattering potential does not have an exponential decay with radius. This conclusion, which was already reported in previous studies involving simpler sources, has been here confirmed unambiguously by studying the scattering off a fictitious potential, the Pöschl-Teller potential, which however decays exponentially with radius.

These generic properties of the gravitational-wave emission coming from black holes perturbed by extended sources represent important differences with respect to corresponding properties of signals produced by very compact sources, such as point-like particles. Of course this conclusion prevents from the derivation of a simple and generic description of the gravitational-wave signal which would be independent of the properties of the perturbing source, but it also opens the exciting perspective of deducing many of the physical properties of the source through a careful analysis of the waveforms produced.

Overall, the results presented here make us confident that the black hole QNM contributions to the full gravitational-wave signal should be extremely small in generic astrophysical scenarios involving the accretion of extended distributions

of matter. On the other hand, it should also be stressed that the time-domain analysis carried out here may not be the most accurate to extract the contributions coming from the perturbed black hole when these are several orders of magnitude smaller than those coming from the source itself or from the backscattering off the potential. In these cases, however, a hybrid approach such as the one proposed in Ref. [19], combining the solution in the time-domain for the hydrodynamics with one in the frequency-domain for the perturbative equations, may be better suited.

Acknowledgments

It is a pleasure to thank E. Berti, H.R. Beyer, S. Bernuzzi, R. De Pietri, I. Olabarrieta, A. Tartaglia and M. Tiglio for

useful discussions and comments. Part of this work was carried out by AN through visits in Valencia and at the Center of Computation and Technology (CCT) at Louisiana State University; the support of the Della Riccia Foundation, of CCT and of ILIAS is gratefully acknowledged. JAF acknowledges financial support from the Spanish *Ministerio de Educación y Ciencia* (grant AYA 2004-08067-C03-01). The computations were performed on the cluster for numerical relativity “Albert” at the University of Parma.

-
- [1] S. Chandrasekhar, *The mathematical theory of black holes*, (Oxford University Press, Oxford, 1992).
 - [2] K.D. Kokkotas and B. Schmidt, *Quasi-normal modes of stars and black holes*, Living Rev. Relativity, Pub. No. lrr-1999-2.
 - [3] V.P. Frolov and I.D. Novikov, *Black Hole Physics*, Kluwer Academic Publishers, Dordrecht 1998.
 - [4] W.H. Press, *Astrophys. J. Letters* **170**, L105 (1971).
 - [5] C.V. Vishveshwara, *Nature (London)*, **227**, 936 (1970).
 - [6] E.W. Leaver, *Phys. Rev. D* **34**, 384 (1986); errata, *Phys. Rev. D* **38**, 725 (1988).
 - [7] N. Andersson, *Phys. Rev. D* **51**, 353 (1995), **52**, 1808 (1995), **55**, 468 (1997).
 - [8] C.O. Lousto and R.H. Price, *Phys. Rev. D* **55**, 2124 (1997).
 - [9] C.T. Cunningham, R.H. Price, and V. Moncrief, *Astrophys. J.*, **224**, 643 (1978).
 - [10] E. Seidel, *Phys. Rev. D* **44**, 950 (1991).
 - [11] L. Baiotti, I. Hawke, L. Rezzolla and E. Schnetter, *Phys. Rev. Lett.* **94**, 131101 (2005).
 - [12] L. Baiotti and L. Rezzolla, *Phys. Rev. Lett.* **97**, 141101 (2006).
 - [13] F. Pretorius, *Phys. Rev. Lett.* **95**, 121101 (2005).
 - [14] M. Campanelli, C.O. Lousto, P. Marronetti, and Y. Zlochower, *Phys. Rev. Lett.* **96**, 111101 (2006).
 - [15] J.G. Baker, J. Centrella, D.I. Choi, M. Koppitz, and J. van Meter, *Phys. Rev. Lett.* **96**, 111102 (2006).
 - [16] P. Papadopoulos and J.A. Font, *Phys. Rev. D* **59**, 044014 (1999).
 - [17] A. Nagar, G. Diaz, J.A. Pons, and J.A. Font, *Phys. Rev. D* **69**, 124028 (2004).
 - [18] A. Nagar, J.A. Font, O. Zanotti and R. De Pietri, *Phys. Rev. D* **72**, 024007 (2005).
 - [19] V. Ferrari, L. Gualtieri and L. Rezzolla, *Phys. Rev. D* **73**, 124028 (2006).
 - [20] S.L. Shapiro and I. Wasserman, *Astrophys. J.* **260**, 838 (1982).
 - [21] L.I. Petrich, S.L. Shapiro and I. Wasserman, *Astrophys. J.* **58**, 297 (1985).
 - [22] H. Sotani and M. Saijo, *Phys. Rev. D* **74**, 024001 (2006).
 - [23] K. Martel and E. Poisson, *Phys. Rev. D* **66**, 084001 (2001).
 - [24] M. Abramowicz, M. Jaroszyński and M. Sikora, *Astron. Astrophys.* **63**, 221 (1978).
 - [25] J.A. Font and F. Daigne, *Mon. Not. R. Astron. Soc.* **334**, 383 (2002).
 - [26] O. Zanotti, L. Rezzolla, and J.A. Font, *Mon. Not. R. Astron. Soc.* **341**, 832 (2003).
 - [27] O. Zanotti, J.A. Font, L. Rezzolla, and P. J. Montero, *Mon. Not. R. Astron. Soc.* **356**, 1371 (2005).
 - [28] L. Rezzolla, T. W. Maccarone, S'i. Yoshida and O. Zanotti, *Mon. Not. Roy. Ast. Soc.* **344**, L37 (2003).
 - [29] L. Rezzolla, S'i. Yoshida and O. Zanotti, *Mon. Not. Roy. Ast. Soc.* **344**, 978 (2003).
 - [30] A. Nagar and L. Rezzolla, *Class. Q. Grav.* **22**, R167 (2005).
 - [31] K. Martel and E. Poisson, *Phys. Rev. D* **71**, 104003 (2005).
 - [32] T. Regge and J.A. Wheeler, *Phys. Rev.* **108**, 1063 (1957).
 - [33] F.J. Zerilli, *Phys. Rev. D* **2**, 2141 (1970).
 - [34] V. Moncrief, *Ann. Phys. (N.Y.)* **88**, 323 (1974).
 - [35] O. Sarbach and M. Tiglio, *Phys. Rev. D* **64**, 084016 (2001).
 - [36] J.N. Goldberg, J. MacFarlane, E.T. Newman, F. Rohrlich and E.C.G. Sudarsahn, *J. Math. Phys.* **8**, 2155 (1967).
 - [37] U.H. Gerlach and U.K. Sengupta, *Phys. Rev. D* **19**, 2268 (1979); **22**, 1300 (1980); J.M. Martín-García and C. Gundlach, *Phys. Rev. D* **59**, 064031 (1999); C. Gundlach and J.M. Martín-García, *Phys. Rev. D* **61**, 084024 (2000); J.M. Martín-García and C. Gundlach, *Phys. Rev. D* **64**, 024012 (2001).
 - [38] J.A. Font, *Numerical Hydrodynamics in General Relativity*, Living Rev. Relativity, Pub. No. lrr-2003-4.
 - [39] S.R. Lau, *J. Math. Phys.* **46**, 102503 (2005).
 - [40] G. Pöschl and E. Teller, *Z. Phys.* **83**, 143 (1933).
 - [41] H.R. Beyer, *Commun. Math. Phys.* **204**, 397 (1999).
 - [42] V. Ferrari and B. Mashhoon, *Phys. Rev. D*, **30**, 295 (1984).
 - [43] E.W. Leaver, *Proc. R. Soc. Lond. A.*, **402**, 285 (1985).
 - [44] R.H. Price, *Phys. Rev. D* **5**, 2419 (1972); **5**, 2439 (1972).
 - [45] E. Berti, V. Cardoso and C. M. Will, in the Proceedings of the VII International Conference of the Hellenic Astronomical Society, *gr-qc/0601077*.
 - [46] A. Nagar, T. Damour and A. Tartaglia, to appear in the special issue of Classical and Quantum Gravity based around the New Frontiers in Numerical Relativity meeting, Albert Einstein Institute, Golm, July 17-21, 2006; *gr-qc/0612096*.
 - [47] M. Davis, R. Ruffini, W.H. Press, and R.H. Price, *Phys. Rev. Lett.* **27**, 1466 (1971); M. Davis, R. Ruffini and J. Tiomno, *Phys. Rev. D* **5**, 2932 (1972).
 - [48] Note that because $\Psi^{(e)}$ is initially nonzero close to the peak of the Zerilli potential, some backscattering is also possible before the bulk of the shell reaches the peak of the potential itself. This explains the small oscillation in the waveform at $u/M \sim 20$.
 - [49] The interested reader is addressed to Paper I and to Ref. [46] for

details about the handling of a point-like particle in the current framework.

- [50] This approach has been systematically adopted in Refs. [8, 23] for a particle plunging radially from a finite distance
- [51] Note that because the system is axisymmetric, $\Psi_{l0}^{(e/o)} = 0$

when $m \neq 0$, and $\Psi_{20}^{(e)} \gg \Psi_{20}^{(o)} \approx 0$, $\Psi_{30}^{(o)} \gg \Psi_{30}^{(e)} \approx 0$.

- [52] It should be noted that the QNM contribution is indeed more than four orders of magnitude smaller in energy than the one coming from the torus.